INTERNATIONAL JOURNAL FOR NUMERICAL METHODS IN FLUIDS
Int. J. Numer. Meth. Fluids 2002; **40**:1187–1207 (DOI: 10.1002/fld.416)

Weighted average flux method and flux limiters for the numerical simulation of shock waves in rigid porous media

R. Torrens and L. C. Wrobel*,†

Department of Mechanical Engineering, Brunel University, Uxbridge UB8 3PH, U.K.

SUMMARY

The one-dimensional flow field generated by the passage of a shock wave in a rigid, thermoelastic porous foam has been simulated using a two-phase mathematical model. The work presented here makes use of the weighted average flux method to solve the system of six equations that govern the problem. Spurious oscillations are eliminated through the application of total variation diminishing limiting methods. Four different limiters were tested: van Leer, SuperA, MinA and van Albada. Numerical tests were carried out to verify the performance of each flux limiter in terms of accuracy. The results were compared to analytical and previously obtained data to assess the performance of the mathematical model. Excellent agreement was obtained. Copyright © 2002 John Wiley & Sons, Ltd.

KEY WORDS: shock wave; rigid porous media; Riemann problem; weighted average flux; TVD

INTRODUCTION

Many experimental and theoretical studies have been carried out in the field of wave propagation in porous media. One of the earliest was performed by Biot [1], who looked at formulating microscopic representations of compressive wave propagation utilizing the theory of mixtures. Many other studies have followed in the wake of Biots' initial work, the majority of which tended to concentrate on the propagation of weak acoustic waves. However, of primary interest in this research is the propagation of non-linear waves, such as shock waves, in porous media.

Early work in this field was carried out by Rogg *et al.* [2], who examined the effect of a porous medium on shock. This was achieved by using experimental shock tube simulation and by solving balance equations for the solid and fluid phases, introducing empirical drag laws for high Reynolds number flows developed by Ergun [3]. The porous medium used in this experimental work consisted of a packed bed of glass beads. This was consistent with the laws

* Correspondence to: L. C. Wrobel, Department of Mechanical Engineering, Brunel University, Uxbridge UB8 3PH, Middlesex, U.K.
† E-mail: luiz.wrobel@brunel.ac.uk

Received November 2000
Revised 24 June 2002

developed by Ergun, but did not provide scope for shock propagation in more generalized porous media.

The foundations of such a method were laid out by Sorek *et al.* [4], in which macroscopic balance equations for mass, momentum and energy are formulated for the fluid and solid phases. This is achieved by treating the porous medium as a continuum, and applying the multiphase approach. Macroscopic balance equations were obtained by averaging the microscopic balance equations over a representative elementary volume (REV), as described by Bear and Bachmat [5].

This idea was advanced further by Levy *et al.* [6], by performing a dimensional analysis on the resulting macroscopic balance equation developed by Sorek *et al.* [4] and Bear *et al.* [7]. This established a theoretical basis on which to model non-linear wave motion in a deformable porous media represented by a continuum of interacting solid and fluid phases. This theoretical model was used as a basis to formulate the set of governing equations for a rigid porous medium. A numerical solution for this problem was proposed and implemented by Levy *et al.* [8] and Ben-Dor *et al.* [9]. The numerical results were validated using experimental results obtained in a previous experimental study carried out by Levy *et al.* [10].

Levy *et al.* [8] describe a numerical solution of a one-dimensional inviscid model for compaction wave propagation in a rigid porous medium. The accuracy of the solution was improved using the TVD method of Harten [11]. The work presented in this paper makes use of the weighted average flux (WAF) method of Toro [12] to circumvent the first-order accuracy restriction placed on monotone numerical methods. There were two reasons why this technique was chosen instead of the method of Levy *et al.* [8]. Firstly, the implementation of the WAF method was thought to be straightforward, and to easily lead itself to the application of a number of TVD flux limiter functions. Secondly, to the best of the authors' knowledge, the WAF method has not been applied to this problem before.

GOVERNING EQUATIONS

The formulation of the three-dimensional macroscopic balance equations for mass, momentum and energy is shown in Levy *et al.* [8], and is based on averaging of the conserved quantities in the microscopic balance over a REV. For the purposes of the two-phase modelling, the REV is treated as a continuum whose porosity is given by

$$\phi = 1 - \frac{\rho_{\text{bulk}}}{\rho_{\text{S}}} \tag{1}$$

where ρ_{bulk} is the bulk density of the porous medium and ρ_{s} is the density of the skeletal solid.

The following assumptions are used in the formulation of the model:

- The fluid is inviscid.
- Diffusive fluxes may be neglected as advective fluxes are much larger.
- There is no coupling between the fluid mass and the solid mass phases.
- The solid matrix may only deform by small amounts.
- The solid matrix is thermoelastic.
- The material from which the solid is made is incompressible.
- The process is adiabatic.

The one-dimensional form of the macroscopic balance equations, along with the constitutive relationships for stress and strain in the solid matrix and the behaviour of the gas, are given in the form:

Mass:

$$\frac{\partial \phi \rho_{\mathrm{f}}}{\partial t} + \frac{\partial \phi \rho_{\mathrm{f}} u_{\mathrm{f}}}{\partial x} = 0 \tag{2}$$

$$\frac{\partial (1-\phi) \rho_{\mathrm{s}}}{\partial t} + \frac{\partial (1-\phi) \rho_{\mathrm{s}} u_{\mathrm{s}}}{\partial x} = 0 \tag{3}$$

where u_n and ρ_n are the velocity and density in the nth phase, where n may be s or f which refer to the solid and the fluid phases, respectively.

Momentum:

$$\frac{\partial \phi \rho_{\mathrm{f}} u_{\mathrm{f}}}{\partial t} + \frac{\partial \phi \rho_{\mathrm{f}} u_{\mathrm{f}}^2}{\partial x} = -C_{\mathrm{T}} \frac{\partial \phi P}{\partial x} + C_{\mathrm{T}} P \frac{\partial \phi}{\partial x} - C_{\mathrm{F}} \phi \rho_{\mathrm{f}} |u_{\mathrm{f}} - u_{\mathrm{s}}| (u_{\mathrm{f}} - u_{\mathrm{s}}) \tag{4}$$

$$\frac{\partial (1-\phi) \rho_{\mathrm{s}} u_{\mathrm{s}}}{\partial t} + \frac{\partial (1-\phi) \rho_{\mathrm{s}} u_{\mathrm{s}}^2}{\partial x} = -C_{\mathrm{T}} \frac{\partial (1-\phi) P}{\partial x} + \frac{\partial \sigma_{\mathrm{s}}'}{\partial x} - C_{\mathrm{T}} P \frac{\partial \phi}{\partial x} + C_{\mathrm{F}} \phi \rho_{\mathrm{f}} |u_{\mathrm{f}} - u_{\mathrm{s}}| (u_{\mathrm{f}} - u_{\mathrm{s}}) \tag{5}$$

where P is the pressure, C_{T} is the tortuosity constant describing the directional cosines of the fluid path through the porous medium, and C_{F} is the Forchheimer constant.

Energy:

$$\frac{\partial \phi \rho_{\mathrm{f}} (c_{\mathrm{f}} T_{\mathrm{f}} + \frac{1}{2} u_{\mathrm{f}}^2)}{\partial t} + \frac{\partial \phi \rho_{\mathrm{f}} u_{\mathrm{f}} (c_{\mathrm{f}} T_{\mathrm{f}} + \frac{1}{2} u_{\mathrm{f}}^2)}{\partial x} = -C_{\mathrm{T}} \frac{\partial \phi u_{\mathrm{f}} P}{\partial x} + C_{\mathrm{T}} P \frac{\partial \phi}{\partial x} - C_{\mathrm{F}} \phi \rho_{\mathrm{f}} |u_{\mathrm{f}} - u_{\mathrm{s}}| (u_{\mathrm{f}} - u_{\mathrm{s}}) u_{\mathrm{s}} \tag{6}$$

$$\frac{\partial (1-\phi) \rho_{\mathrm{s}} (c_{\mathrm{s}} T_{\mathrm{s}} + \frac{1}{2} u_{\mathrm{s}}^2)}{\partial t} + \frac{\partial (1-\phi) \rho_{\mathrm{s}} u_{\mathrm{s}} (c_{\mathrm{s}} T_{\mathrm{s}} + \frac{1}{2} u_{\mathrm{s}}^2)}{\partial x} = -C_{\mathrm{T}} \frac{\partial (1-\phi) u_{\mathrm{s}} P}{\partial x} + \frac{\partial u_{\mathrm{s}} \sigma_{\mathrm{s}}'}{\partial x} - C_{\mathrm{T}} P \frac{\partial \phi}{\partial x} + C_{\mathrm{F}} \phi \rho_{\mathrm{f}} |u_{\mathrm{f}} - u_{\mathrm{s}}| (u_{\mathrm{f}} - u_{\mathrm{s}}) u_{\mathrm{s}} \tag{7}$$

where T_n and c_n are the temperature and specific heat capacity at constant volume in the nth phase.

The effective stress in the solid matrix may be expressed in the following form:

$$\sigma_{\mathrm{s}}' = E_{\varepsilon} \varepsilon - E_{\mathrm{T}} c_{\mathrm{s}} (T_{\mathrm{s}} - T_{\mathrm{s}0}) \tag{8}$$

Driver Section	Driven Section
P = 801325 Pa, T = 300K	P = 101325 Pa, T = 300K

Figure 1. Initial conditions for simulation.

where E_ε and E_T are the Lamé constants for the solid matrix, T_{s0} is its initial temperature and ε, the macroscopic strain as a function of porosity, is defined by

$$\varepsilon = 1 - \frac{r_s}{r_{s0}}$$

where r_{s0} is the initial mass fraction of the solid.

Finally, the second constitutive law—the equation of state for the fluid—is written in the form

$$P = \rho_f R T_f \tag{9}$$

where R is the gas constant for air.

SOLUTION STRATEGY

When the gradient of porosity is small, Equations (2)–(7) form a coupled, hyperbolic system of equations that may be used to describe the fluid flow in the porous media following an abrupt change in flow variables (i.e. a shock wave). The familiar shock tube problem was used as the initial value problem. Figure 1 shows a schematic of a shock tube with initial conditions defined either side of the diaphragm.

The shock tube problem is a specific case of the more general Riemann problem, which describes discontinuities in initial data applied to hyperbolic equations. Toro [12] gives an excellent account of many of the methods that have been developed to solve this problem. The method of Roe is used in this work to solve the Riemann problem, to calculate the intercellular fluxes and jumps that are needed to update the solution. Roe's method makes use of an explicit formulation of the eigenvalues, right eigenvectors and wave strengths of the Jacobian matrix of the system of governing equations. In order to find these values, it is necessary to reformulate Equations (2)–(7) in the form:

$$\mathbf{U}_t + [\mathbf{F}(\mathbf{U})]_x = \mathbf{Q} \tag{10}$$

Levy *et al.* [8] describe the conserved variables using the following definitions:

$$r_f = \phi\rho_f, \quad m_f = r_f u_f, \quad E_f = r_f(c_f T_f + \tfrac{1}{2}u_f^2)$$

$$r_s = (1-\phi)\rho_s, \quad m_s = r_s u_s, \quad E_s = r_s(c_s T_s + \tfrac{1}{2}u_s^2)$$

This allows the conserved variables, fluxes and sources, to be written in the form:

Conserved variable vector:

$$\mathbf{U} = [r_f, r_s, m_f, m_s, E_f, E_s]^T \tag{11}$$

Flux vector:

$$\mathbf{F}=\begin{bmatrix} m_{\mathrm{f}} \\ m_{\mathrm{s}} \\ \dfrac{m_{\mathrm{f}}^2}{r_{\mathrm{f}}}+C_{\mathrm{T}}\phi P \\ \dfrac{m_{\mathrm{s}}^2}{r_{\mathrm{s}}}-\sigma_{\mathrm{s}}'+(1-C_{\mathrm{T}}\phi)P \\ \dfrac{m_{\mathrm{f}}}{r_{\mathrm{f}}}(E_{\mathrm{f}}+C_{\mathrm{T}}\phi P) \\ \dfrac{m_{\mathrm{s}}}{r_{\mathrm{s}}}(E_{\mathrm{s}}-\sigma_{\mathrm{s}}'+(1-C_{\mathrm{T}}\phi)P) \end{bmatrix} \tag{12}$$

Source vector:

$$\mathbf{Q}=\begin{bmatrix} 0 \\ 0 \\ C_{\mathrm{T}}P\dfrac{\partial\phi}{\partial x}-C_{\mathrm{F}}r_{\mathrm{f}}\left|\dfrac{m_{\mathrm{f}}}{r_{\mathrm{f}}}-\dfrac{m_{\mathrm{s}}}{r_{\mathrm{s}}}\right|\left(\dfrac{m_{\mathrm{f}}}{r_{\mathrm{f}}}-\dfrac{m_{\mathrm{s}}}{r_{\mathrm{s}}}\right) \\ -C_{\mathrm{T}}P\dfrac{\partial\phi}{\partial x}+C_{\mathrm{F}}r_{\mathrm{f}}\left|\dfrac{m_{\mathrm{f}}}{r_{\mathrm{f}}}-\dfrac{m_{\mathrm{s}}}{r_{\mathrm{s}}}\right|\left(\dfrac{m_{\mathrm{f}}}{r_{\mathrm{f}}}-\dfrac{m_{\mathrm{s}}}{r_{\mathrm{s}}}\right) \\ \dfrac{m_{\mathrm{s}}}{r_{\mathrm{s}}}\left(C_{\mathrm{T}}P\dfrac{\partial\phi}{\partial x}-C_{\mathrm{F}}r_{\mathrm{f}}\left|\dfrac{m_{\mathrm{f}}}{r_{\mathrm{f}}}-\dfrac{m_{\mathrm{s}}}{r_{\mathrm{s}}}\right|\left(\dfrac{m_{\mathrm{f}}}{r_{\mathrm{f}}}-\dfrac{m_{\mathrm{s}}}{r_{\mathrm{s}}}\right)\right) \\ \dfrac{m_{\mathrm{s}}}{r_{\mathrm{s}}}\left(-C_{\mathrm{T}}P\dfrac{\partial\phi}{\partial x}+C_{\mathrm{F}}r_{\mathrm{f}}\left|\dfrac{m_{\mathrm{f}}}{r_{\mathrm{f}}}-\dfrac{m_{\mathrm{s}}}{r_{\mathrm{s}}}\right|\left(\dfrac{m_{\mathrm{f}}}{r_{\mathrm{f}}}-\dfrac{m_{\mathrm{s}}}{r_{\mathrm{s}}}\right)\right) \end{bmatrix} \tag{13}$$

The Jacobian matrix $\mathbf{A}(\mathbf{U})=\partial\mathbf{F}(\mathbf{U})/\partial\mathbf{U}$ was formed using Mathematica. From this, the six eigenvalues, right eigenvectors and wave strengths may be found symbolically. These are shown in Appendix A.

The eigenvectors are all real and distinct, hence the problem posed by (10) is strictly hyperbolic. Each eigenvector/eigenvalue/wave strength combination may be associated with a wave, as shown in Figure 2. This provides a means by which the flux jumps across the waves may be directly approximated using Roe's method

$$\Delta\mathbf{F}=\mathbf{F}_{\mathbf{R}}-\mathbf{F}_{\mathbf{L}}=\sum_{k=1}^{6}\tilde{\alpha}_k\tilde{\lambda}_k\tilde{\mathbf{R}}^{(k)} \tag{15}$$

where $\tilde{\alpha}_k$, $\tilde{\lambda}_l$ and $\tilde{\mathbf{R}}^{(k)}$ are the Roe averaged wave strength, eigenvalue and eigenvector associated with the kth wave. The Harten–Hyman entropy fix [12] was applied during the calculation of the Roe averaged flux jumps. The formulation of the Roe averaged quantities is given in Appendix A.

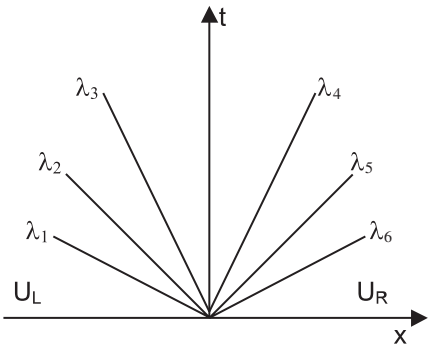

Figure 2. Wave structure.

NUMERICAL METHOD

A fully explicit discrete formulation of (10) was used to time step the initial value problem, in the form

$$\mathbf{U}_i^{n+1} = \mathbf{U}_i^n + \frac{\Delta t}{\Delta x}(\mathbf{F}_{i-1/2}^n - \mathbf{F}_{i+1/2}^n) + \Delta t \mathbf{Q}_i \tag{16}$$

The intercellular fluxes are calculated by solving the local Riemann problem between nodes i and $i+1$. Once found, they may be used to update the solution at time $n+1$ using Equation (16). The WAF method was used to calculate the Riemann fluxes. The WAF is defined in integral form by Toro [12] as

$$\mathbf{F}_{i+1/2} = \int_{-\Delta x/2}^{\Delta x/2} \mathbf{F}\left(\mathbf{U}_{i+1/2}\left(x, \frac{\Delta t}{2}\right)\right) \mathrm{d}x \tag{17}$$

Using the known information about the wave structure shown in Figure 2, and making use of the wave jump values found using Equation (15), Equation (17) may be written in the form

$$\mathbf{F}_{i+1/2} = \frac{1}{2}(\mathbf{F}_i + \mathbf{F}_{i+1}) - \frac{1}{2}\sum \mathrm{sgn}(c_k)\phi_{i+1/2}^k \Delta \mathbf{F}_{i+1/2}^{(k)} \tag{18}$$

where c_k is the wave Courant number, $\phi_{i+1/2}^k$ is the WAF limiter function and the function sgn() is equal to one or minus one, depending on the sign of c_k. Flux (18) is used in Equation (16) to update the solution to the next time level.

TVD FLUX LIMITER FUNCTIONS

The flux limiter function, $\phi_{i+1/2}^k$, shown in Equation (18), was used to apply a TVD condition to the flux. Separate limiters are calculated for the flux jumps across each wave. Table I details the flux limiter functions used to apply the TVD condition. In each case, the limiters are functions of r, which is the ratio of local to upwind solid energy jumps across the

Table I. Flux limiters.

First order	$\phi(r)=1$
van Leer	$\phi(r)=\begin{cases}1 & \text{if } r\leqslant 0\\ 1-\dfrac{(1-\lvert c\rvert)2r}{1+r} & \text{if } r\geqslant 0\end{cases}$
SuperA	$\phi(r)=\begin{cases}1 & \text{if } r\leqslant 0\\ 1-2(1-\lvert c\rvert)r & \text{if } 0\leqslant r\leqslant \frac{1}{2}\\ \lvert c\rvert & \text{if } \frac{1}{2}\leqslant r\leqslant 1\\ 1-(1-\lvert c\rvert)r & \text{if } 1\leqslant r\leqslant 2\\ 2\lvert c\rvert-1 & \text{if } r\geqslant 2\end{cases}$
MinA	$\phi(r)=\begin{cases}1 & \text{if } r\leqslant 0\\ 1-(1-\lvert c\rvert)r & \text{if } 0\leqslant r\leqslant 1\\ \lvert c\rvert & \text{if } r\geqslant 1\end{cases}$
van Albada	$\phi(r)=\begin{cases}1 & \text{if } r\leqslant 0\\ 1-\dfrac{(1-\lvert c\rvert)r(1+r)}{(1+r)^2} & \text{if } r\geqslant 0\end{cases}$

respective wave

$$r_k=\frac{E_s^{k+1}-E_s^k|_{i-1/2}}{E_s^{k+1}-E_s^k|_{i+1/2}} \tag{19}$$

The solid energy was chosen for two reasons: firstly, it changes across all waves on the solution x–t domain and, secondly, because the results obtained during the simulations appeared smoother without loss of accuracy. For obvious reasons, fluid-only simulations require a fluid parameter to be used in the calculation of r. The fluid mass was used in this case.

The first limiter shown in Table I results in a first-order accurate flux. The van Leer, SuperA, van Albada and MinA functions limit the amount of downwinding utilized by the WAF method. This aims to eliminate the smearing of wave fronts associated with the first-order method, and to prevent the spurious oscillations associated with centred second-order methods (i.e. Lax Wendroff).

NUMERICAL TESTS

Two numerical tests were performed. The first tested the performance of the flux limiters in Table I for the shock tube problem in a single-phase fluid medium. The second tested the limiters performance for the two-phase homogeneous rigid porous foam. Figure 3 shows the initial conditions used in both tests.

The simulation of the porous medium requires the definition of several material constants (two of which are shown in Figure 3: porosity and specific heat capacity). These are the Forchheimer and tortuosity constants, the Lamé coefficients and the density of the skeletal material. Table II shows the values used, which were based on a rigid porous foam called

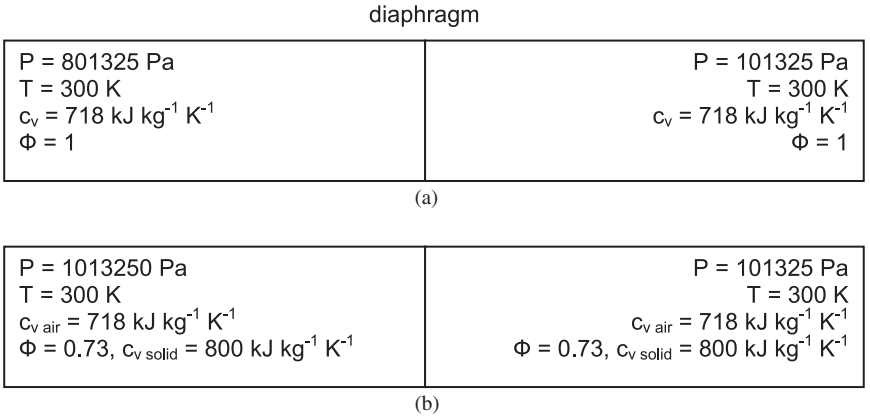

Figure 3. Initial conditions for numerical tests: (a) single-phase fluid only—air; (b) two-phase flow—air saturated porous medium.

Table II. Porous medium material constants.

Forchheimer	C_F	$300\,l\,s^{-1}$
Tortuosity	C_T	0.7
Lamé	E_ε	380×10^7 Pa
	E_T	$26.207\,kg\,m^{-3}$
Density	ρ_s	$2000\,kg\,m^{-3}$

Sivex (manufactured by Pyrotek, Switzerland). The values of the material constants were taken from Levy *et al.* [8, 9].

The time step, Δt, was calculated at each time level using a Courant number of 0.9, as follows:

$$\Delta t = \frac{0.9\Delta x}{S_{MAX}} \tag{20}$$

where S_{MAX} is the maximum wave speed at each time step. The application of this condition ensured that the time step was sufficiently small for the numerical method to remain stable.

The computer code was written in Fortran 90 and executed on a Pentium PC. The spatial domain was 1.6 m in length. The convergence of the numerical methods was verified by running tests for 100, 200 and 500 grid points. All runs took less than one minute of CPU time.

RESULTS

Test 1: fluid medium

The density variation 1 ms after diaphragm burst is shown in Figures 4(a) (100 nodes), 4(b) (200 nodes) and 4(c) (500 nodes). The choice of density as the displayed fluid variable was

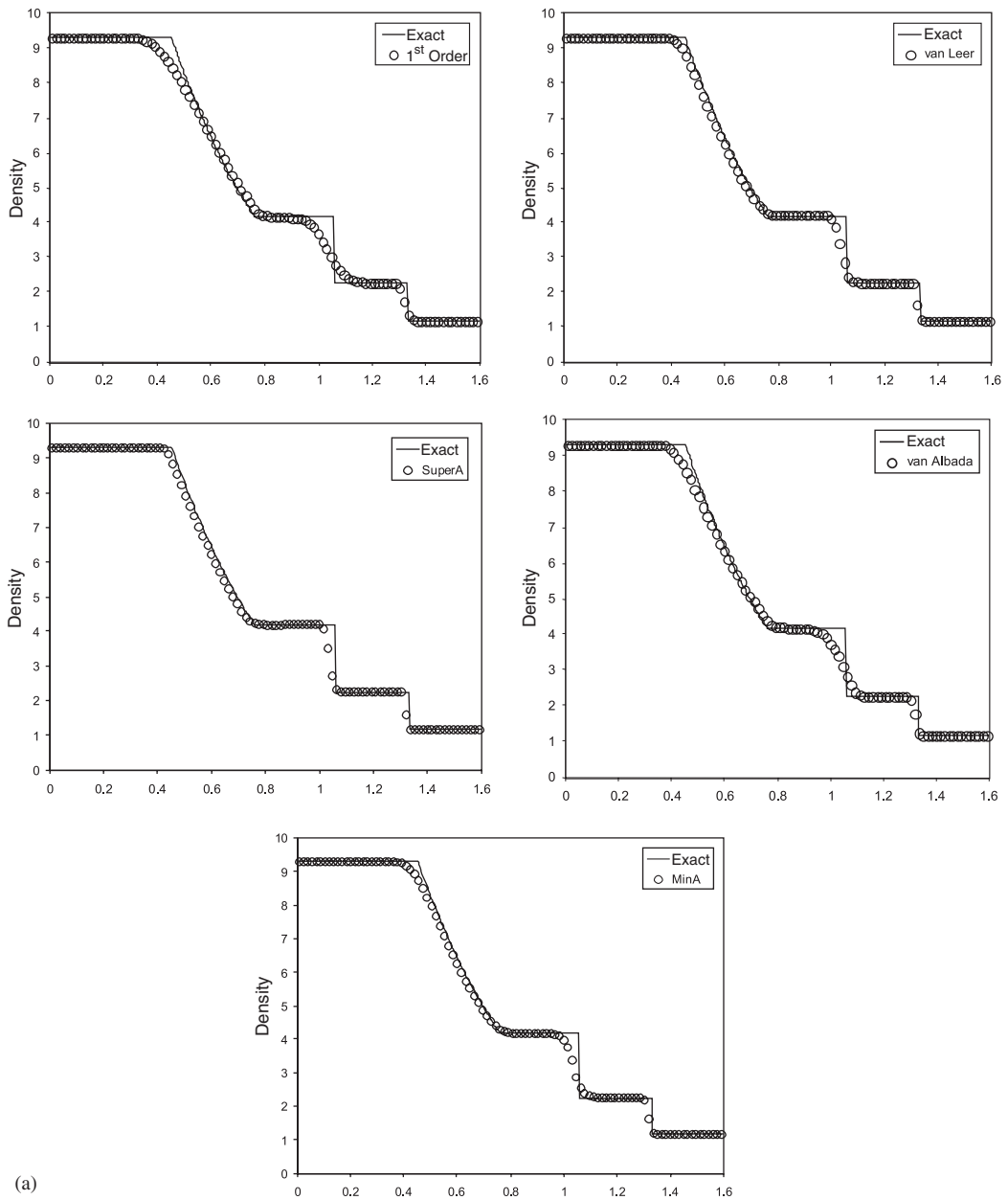

(a)

Figure 4. (a) Density plots for 100 node fluid only solution; (b) density plots for 200 node fluid only solution; (c) density plots for 500 node fluid only solution.

based on the fact that it changes across all waves in the solution field. The advantage of this is that the effects of the WAF flux limiters could be observed across all wave fronts. The plots compare the results of the WAF method using Roe's first-order flux and each of the four TVD flux limiters, against an analytical solution. The most important factors taken into

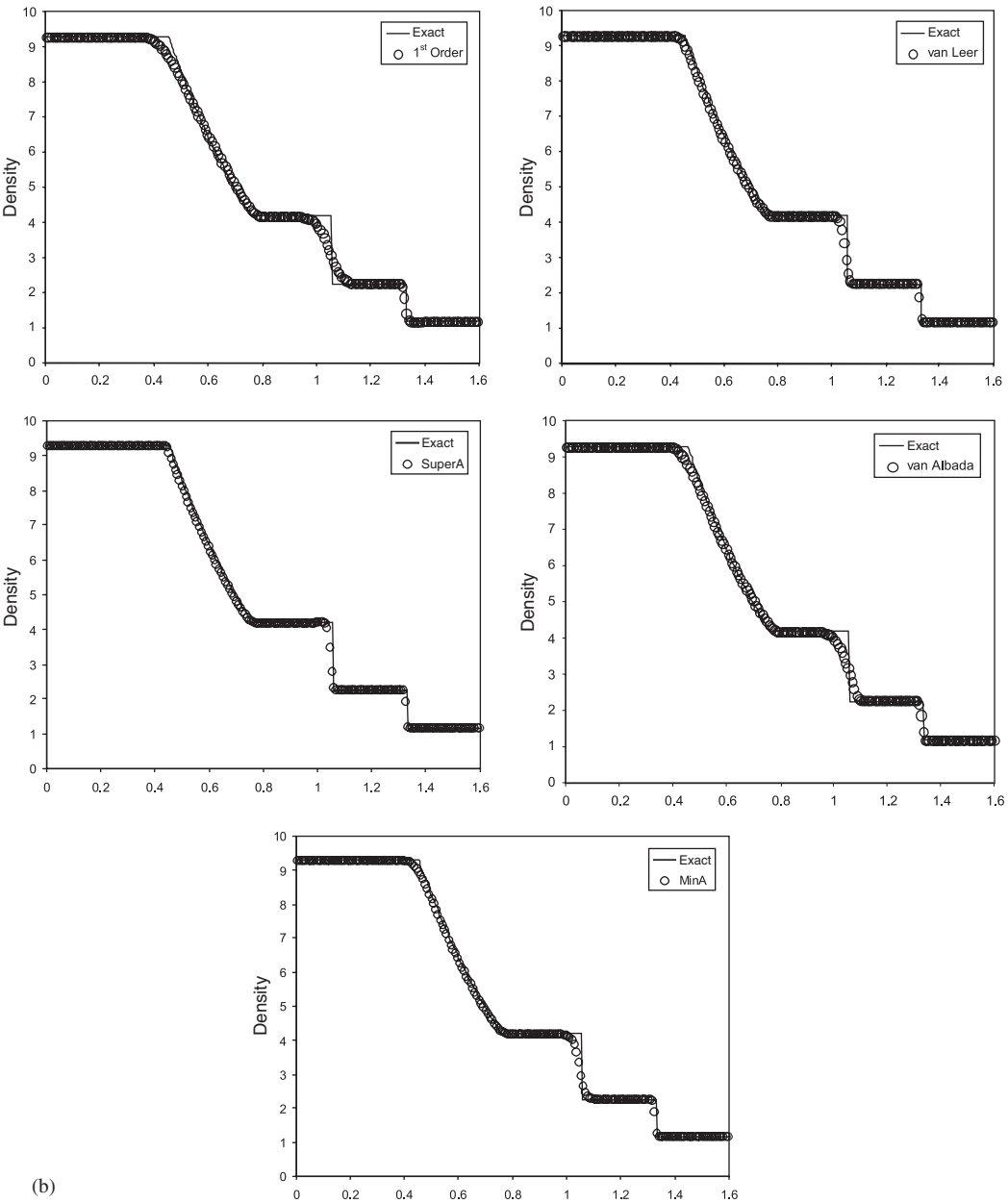

(b)

Figure 4. (*Continued*).

consideration are the resolution of the numerical solution compared to the exact solution, and the convergence of the numerical methods applied.

The van Leer, SuperA and MinA flux limiters exhibit definite advantages over Roe's first-order method. It may be seen that, with the exception of the van Albada limiter, the plots

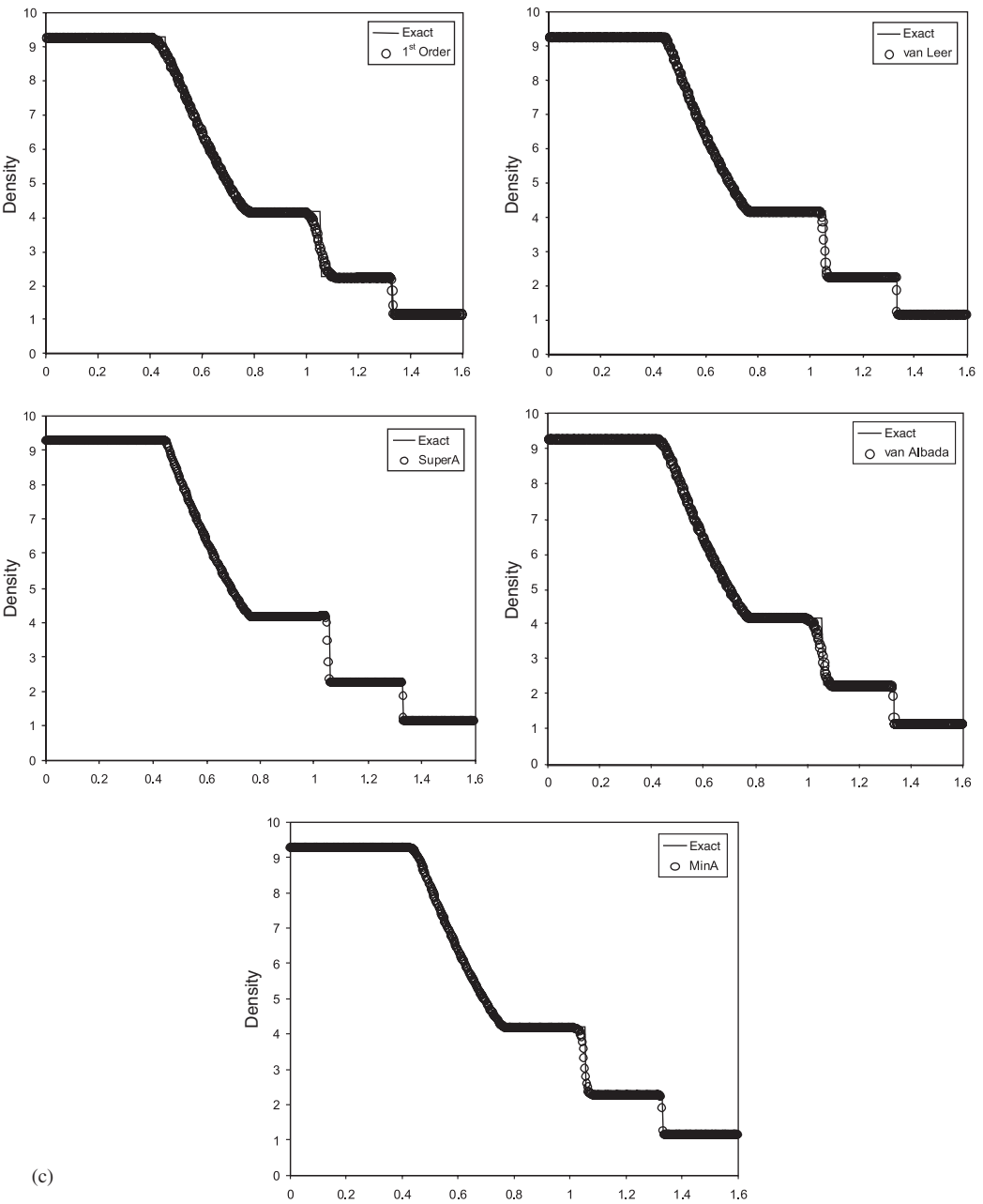

(c)

Figure 4. (*Continued*).

in Figure 4(a)–(c) show that shock and contact waves suffer less from numerical smearing with the TVD flux limiters than with Roe's first-order method, when compared to the exact solution.

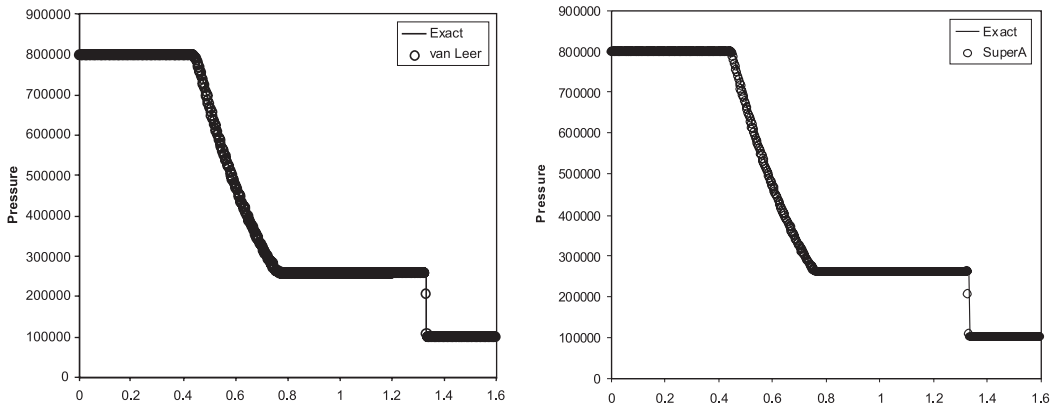

Figure 5. Pressure distribution for fluid only problem.

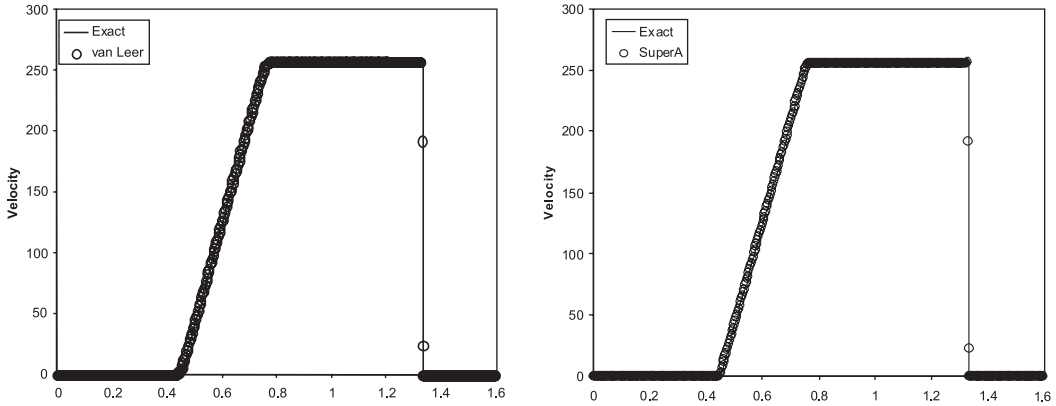

Figure 6. Velocity distribution for fluid only problem.

Figures 5 and 6 show the pressure and velocity distributions in the shock tube after 1 ms for both the van Leer and SuperA flux limiters, using 500 computation nodes. The results compare favourably with the exact solutions in terms of resolution of the shock front. The effect of increasing the number of grid points was, in all cases, to improve the accuracy of the solution.

Test 2: porous medium

The solutions presented for the second set of numerical tests are shown in Figures 7 and 8, at a time 260 μs after diaphragm burst. The speed of sound in the solid matrix is much higher than in the fluid. As a result of this, it was necessary to use a small solution end time to obtain meaningful results. Due to the complexity of this problem, no exact solution was available for comparison.

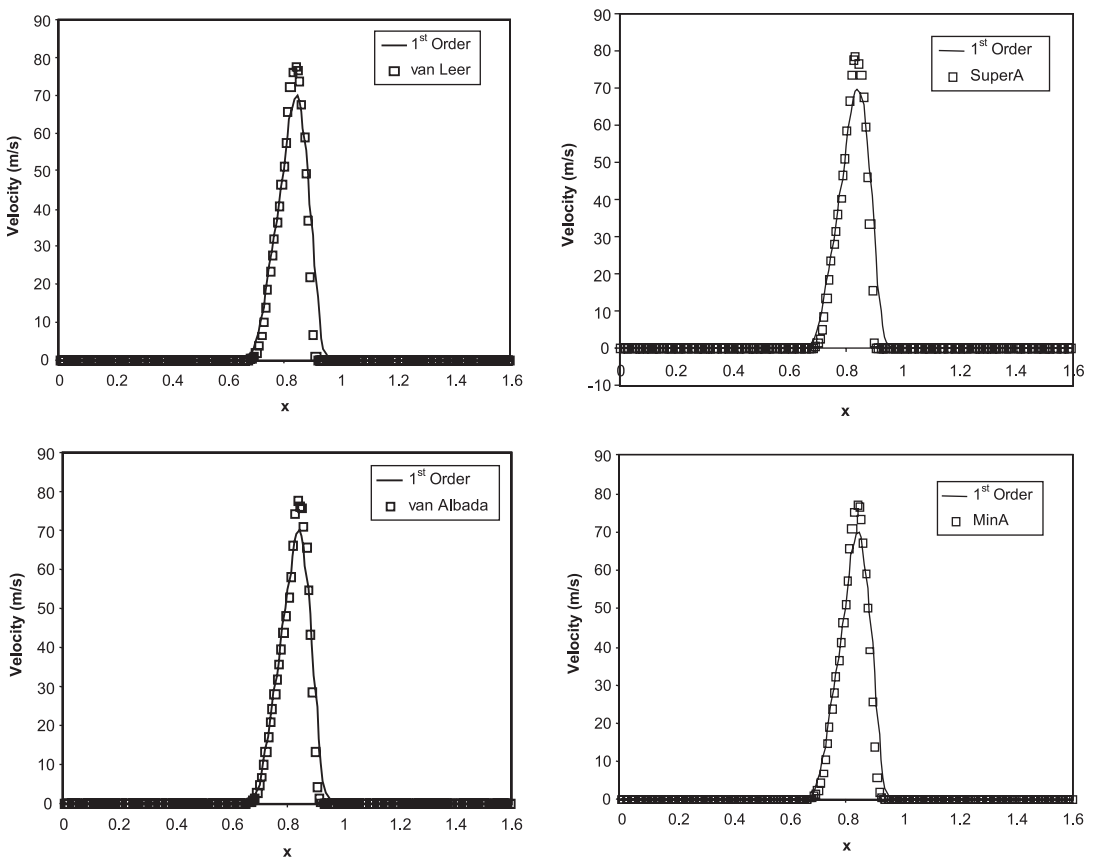

Figure 7. Fluid velocity plots for 200 node porous medium solution.

The fluid velocity plots shown in Figure 7 compare the solutions obtained using the TVD flux limiters and the Roe first-order method. There exists a considerable discrepancy between the results of the first- and second-order methods, due to numerical diffusion. The maximum velocity shown on the second-order distributions is approximately 12% higher in each case.

The results shown in Figure 8 are for the normal stress field in the porous medium. The difference between the TVD flux limiter and the Roe first-order solutions was marginal. The SuperA limiter seemed to offer a small improvement in sharpness, which was not observed for the other three limiters.

Figure 9 shows a comparison between SuperA and van Leer flux limiters for the porosity and pressure distributions in the porous medium. The distributions are virtually identical in each case.

The results obtained were compared with those shown in Ben-Dor *et al.* [9], which were obtained using the same initial conditions, material parameters and end time. Comparisons were drawn between the general curve profile, the height of the curve at its maxima and

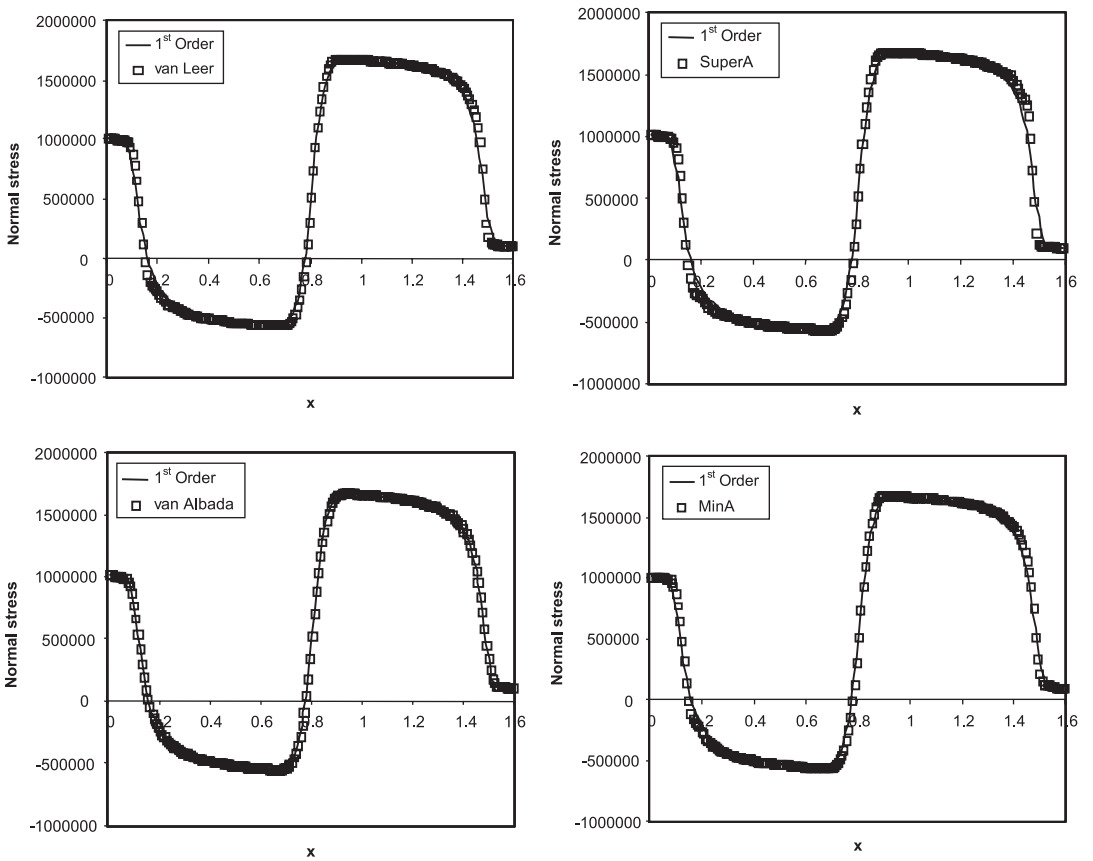

Figure 8. Normal stress plots for 200 node porous medium solution.

the width of curve at its base. All the curve profiles in Figure 7 are similar to the result in Ben-Dor *et al.* [9]. The deviation of the maximum velocity is only 1–2% in the worst case. The main difference lies in the width of the curve base. This was assessed by finding the ratio of the base width to the domain length, for each velocity distribution. Table III shows that the SuperA limiter offers the best performance, compared to that of Ben-Dor *et al.* [9].

CONCLUSIONS

The shock tube problem has been successfully simulated using the WAF method for one- and two-phase flow regimes. The application of TVD flux limiters to improve the accuracy of the numerical method was successful. This improvement manifested itself in terms of better resolution around discontinuities and a lessening of the effects of numerical diffusion associated with the first-order Roe method (see difference in maximum values in Figure 7). The SuperA limiter offered the best performance in terms of improving

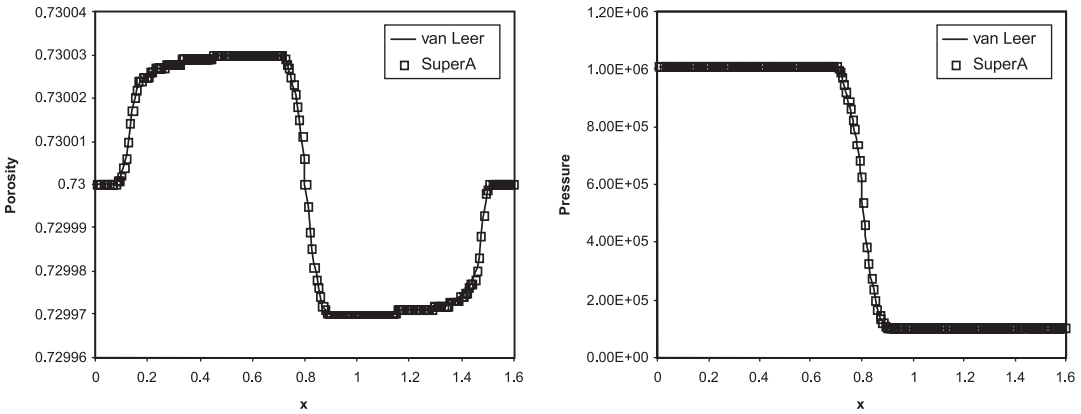

Figure 9. Porosity (a) and pressure (b) distributions for porous medium problem—van Leer and SuperA only.

Table III. Curve base ratio.

Ben-Dor *et al.* [9]	7.75
SuperA	7.61
van Leer	7.38
MinA	6.88
van Albada	6.0

the resolution around the discontinuities, closely followed by the van Leer and MinA limiters.

The present simulation of a shock wave in a porous medium was entirely theoretical. Direct experimental validation of the results was not possible, due to the impracticalities of implementing a bursting mechanism inside the porous medium. Further work will utilize the numerical techniques developed here to model the interaction of a shock wave with a thin layer of porous material mounted in a shock tube. This will allow the results to be experimentally validated.

APPENDIX A

The system of governing Equations (2)–(7) may be written in the form

$$\mathbf{U}_t + \mathbf{A}(\mathbf{U})\mathbf{U}_x = \mathbf{Q} \tag{A1}$$

where the Jacobian is given by

$$\mathbf{A}(\mathbf{U}) = \frac{\partial \mathbf{F}(\mathbf{U})}{\partial \mathbf{U}} \tag{A2}$$

The 6×6 Jacobian may be found symbolically using the software *Mathematica*, and is given by

$$\mathbf{A} = \begin{bmatrix} a_{11} & a_{12} & a_{13} & a_{14} & a_{15} & a_{16} \\ a_{21} & a_{22} & a_{23} & a_{24} & a_{25} & a_{26} \\ a_{31} & a_{32} & a_{33} & a_{34} & a_{35} & a_{36} \\ a_{41} & a_{42} & a_{43} & a_{44} & a_{45} & a_{46} \\ a_{51} & a_{52} & a_{53} & a_{54} & a_{55} & a_{56} \\ a_{61} & a_{62} & a_{63} & a_{64} & a_{65} & a_{66} \end{bmatrix} \tag{A3}$$

The definitions of a_{ij}, where i and j range from one to six, are given below:

First row:

$$a_{11} = 0, \quad a_{12} = 0, \quad a_{13} = 1, \quad a_{14} = 0, \quad a_{15} = 0, \quad a_{16} = 0 \tag{A3a}$$

Second row:

$$a_{21} = 0, \quad a_{22} = 0, \quad a_{23} = 0, \quad a_{24} = 1, \quad a_{25} = 0, \quad a_{26} = 0 \tag{A3b}$$

Third row:

$$a_{31} = \tfrac{1}{2} V_{\mathrm{f}}^2 (T^*(\gamma - 1) - 2), \quad a_{32} = 0, \quad a_{33} = V_{\mathrm{f}}(2 + T^*(1 - \gamma)), \quad a_{34} = 0$$

$$a_{35} = T^*(\gamma - 1), \quad a_{36} = 0 \tag{A3c}$$

Fourth row:

$$\begin{aligned} a_{41} &= -\frac{V_{\mathrm{f}}^2(\gamma - 1)(T^* r_{\mathrm{s}} - (T^* - 1)\rho_{\mathrm{s}})}{2(r_{\mathrm{s}} - \rho_{\mathrm{s}})} \\ a_{42} &= \frac{E_{\varepsilon}}{r_{\mathrm{s}0}} - V_{\mathrm{s}}^2 + \frac{E_{\mathrm{T}}(r_{\mathrm{s}} V_{\mathrm{s}}^2 - E_{\mathrm{s}})}{r_{\mathrm{s}}^2} - \frac{T^*(2E_{\mathrm{f}} - r_{\mathrm{f}} V_{\mathrm{f}}^2)(\gamma - 1)}{2(r_{\mathrm{s}} - \rho_{\mathrm{s}})} \\ &\quad + \frac{(2E_{\mathrm{f}} - r_{\mathrm{f}} V_{\mathrm{f}}^2)(\gamma - 1)(T^* r_{\mathrm{s}} - (T^* - 1)\rho_{\mathrm{s}})}{2(r_{\mathrm{s}} - \rho_{\mathrm{s}})^2} \\ a_{43} &= \frac{V_{\mathrm{f}}(\gamma - 1)(T^* r_{\mathrm{s}} - (T^* - 1)\rho_{\mathrm{s}})}{r_{\mathrm{s}} - \rho_{\mathrm{s}}}, \quad a_{44} = \left(2 - \frac{E_{\mathrm{T}}}{r_{\mathrm{s}}}\right) V_{\mathrm{s}} \\ a_{45} &= -\frac{(\gamma - 1)(T^* r_{\mathrm{s}} - (T^* - 1)\rho_{\mathrm{s}})}{r_{\mathrm{s}} - \rho_{\mathrm{s}}}, \quad a_{46} = \frac{E_{\mathrm{T}}}{r_{\mathrm{s}}} \end{aligned} \tag{A3d}$$

Fifth row:

$$\begin{aligned} a_{51} &= \frac{V_{\mathrm{f}}(r_{\mathrm{f}} T^* V_{\mathrm{f}}^2(\gamma - 1) + E_{\mathrm{f}}(T^*(1 - \gamma) - 1))}{r_{\mathrm{f}}}, \quad a_{52} = 0 \\ a_{53} &= \frac{2E_{\mathrm{f}}(1 + T^*(\gamma - 1)) - 3r_{\mathrm{f}} T^* V_{\mathrm{f}}^2(\gamma - 1)}{2r_{\mathrm{f}}}, \quad a_{54} = 0 \\ a_{55} &= V_{\mathrm{f}}(1 + T^*(\gamma - 1)), \quad a_{56} = 0 \end{aligned} \tag{A3e}$$

Sixth row:

$$
\begin{aligned}
a_{61} &= -\frac{V_f^2 V_s(\gamma-1)(T^* r_s-(T^*-1)\rho_s)}{2(r_s-\rho_s)}\\
a_{62} &= V_s\left(\frac{E_\varepsilon}{r_{s0}}+\frac{E_T(r_s V_s^2-E_s)}{r_s^2}-\frac{T^*(2E_f-r_f V_f^2)(\gamma-1)}{2(r_s-\rho_s)}\right.\\
&\quad+\frac{(2E_f-r_f V_f^2)(\gamma-1)(T^* r_s-(T^*-1)\rho_s)}{2(r_s-\rho_s)^2}\\
&\quad-\frac{(2E_f-r_f V_f^2)(\gamma-1)(r_s T^*-(T^*-1)\rho_s)}{2r_s(r_s-\rho_s)}\\
&\quad\left.+\frac{E_s+E_\varepsilon(r_s-r_{s0})/r+E_T(m_{s0}^2/2r_{s0}^2-E_{s0}/r_{s0}+E_s/r_s+V_s^2/2)}{r_s}\right) \qquad \text{(A3f)}\\
a_{63} &= \frac{V_s V_f(\gamma-1)(T^* r_s-(T^*-1)\rho_s)}{r_s-\rho_s}\\
a_{64} &= \frac{E_s+E_\varepsilon(r_s-r_{s0})/r_{s0}-E_T V_s^2+E_T(m_{s0}^2/2r_{s0}^2-E_{s0}/r_{s0}+E_s/r_s+V_s^2/2)}{r_s}\\
&\quad-\frac{(2E_f-r_f V_f^2)(\gamma-1)(r_s T^*-(T^*-1)\rho_s)}{2r_s(r_s-\rho_s)}\\
a_{65} &= -\frac{V_s(\gamma-1)(T^* r_s-(T^*-1)\rho_s)}{r_s-\rho_s}, \quad a_{66}=\frac{V_s(E_T+r_s)}{r_s}
\end{aligned}
$$

The eigenvalues, also evaluated using *Mathematica*, are of the form:

$$
\begin{aligned}
&\lambda_1 = V_s - a_s, \quad \lambda_2 = V_f - a_f, \quad \lambda_3 = V_s\\
&\lambda_4 = V_f, \quad \lambda_5 = V_f + a_f, \quad \lambda_6 = V_s + a_s
\end{aligned} \qquad \text{(A4)}
$$

where the speed of sound in the fluid, a_f, is given by

$$
a_f = \frac{\phi P(1-T^*+\gamma T)T^*}{r_f} \qquad \text{(A5)}
$$

and the speed of sound in the solid, a_s, is given by

$$
a_s = \sqrt{\frac{E_\varepsilon}{r_{s0}}+\left(\frac{\rho_s}{\rho_s-r_s}+\frac{E_T(\rho_s(1-T^*)+T^* r_s)}{r_s^2}\right)\frac{\phi P}{(\rho_s-r_s)}-\frac{E_T\sigma_s'}{r_s^2}} \qquad \text{(A6)}
$$

Eigenvalues (A4) obtained using *Mathematica* were verified against those obtained by Levy *et al*. [8]. However, the task of reproducing the eigenvectors using *Mathematica* was not as straightforward as for the eigenvalues. Although expressions were successfully computed using *Mathematica*, they were extremely long and complex, and could not be explicitly reconciled

with the eigenvectors of Levy *et al.* [8]. Because of the length of the computed expressions, it was decided to use the more compact forms of Levy *et al.* [8] without explicit verification. This decision was justified by the correct results of the numerical simulations.

The eigenvectors presented by Levy *et al.* [8] are shown below

$$K^{(1)}=\begin{bmatrix}0\\1\\0\\V_s-a_s\\0\\H_s-V_s a_s\end{bmatrix},\quad K^{(2)}=\begin{bmatrix}1\\-\dfrac{a_f^2(\rho_s-(\rho_s-r_s)T^*)}{(a_s^2-\zeta_1^2)(\rho_s-r_s)T^*}\\V_f-a_f\\\dfrac{a_f^2(\rho_s-(\rho_s-r_s)T^*)(\zeta_1-V_s)}{(a_s^2-\zeta_1^2)(\rho_s-r_s)T^*}\\H_f-V_f a_f\\\dfrac{a_f^2(\rho_s-(\rho_s-r_s)T^*)(\zeta_1 V_s-H_s)}{(a_s^2-\zeta_1^2)(\rho_s-r_s)T^*}\end{bmatrix}$$

$$K^{(3)}=\begin{bmatrix}0\\1\\0\\V_s\\0\\H_s-\dfrac{r_s a_s^2}{E_T}\end{bmatrix},\quad K^{(4)}=\begin{bmatrix}1\\0\\V_f\\0\\V_f^2\\0\end{bmatrix}\tag{A7}$$

$$K^{(5)}=\begin{bmatrix}1\\-\dfrac{a_f^2(\rho_s-(\rho_s-r_s)T^*)}{(a_s^2-\zeta_2^2)(\rho_s-r_s)T^*}\\V_f+a_f\\-\dfrac{a_f^2(\rho_s-(\rho_s-r_s)T^*)(\zeta_2+V_s)}{(a_s^2-\zeta_2^2)(\rho_s-r_s)T^*}\\H_f+V_f a_f\\-\dfrac{a_f^2(\rho_s-(\rho_s-r_s)T^*)(\zeta_2 V_s+H_s)}{(a_s^2-\zeta_2^2)(\rho_s-r_s)T^*}\end{bmatrix},\quad K^{(6)}=\begin{bmatrix}0\\1\\0\\V_s+a_s\\0\\H_s+V_s a_s\end{bmatrix}$$

where the enthalpy of the fluid, H_f, is given by

$$H_f=\frac{E_f+T^*\phi P}{r_f}\tag{A8}$$

and the enthalpy of the solid, H_s, is given by

$$H_s = \frac{E_s}{r_s} - \frac{\sigma'_s}{r_s} + \frac{(1-\phi T^*)P}{r_s} \tag{A9}$$

The variables ζ_1 and ζ_2 are defined by

$$\zeta_1 = a_f - V_f + V_s \quad \text{and} \quad \zeta_2 = a_f + V_f - V_s \tag{A10}$$

The number of equations in the system corresponds to the number of waves in the solution. For a linear system of equations, the eigenvalues describe the propagation speed of the waves in the solution, while the eigenvectors relate to the jumps in the conserved variables and fluxes across each wave. However, system (A1) is not linear. Roe's method allows the calculation of flux jumps across the waves in the solution domain, by converting a non-linear system into a quasi-linear system, which approximates the real solution. The process is referred to as Roe linearisation. The system characteristic curves may be plotted on an x–t diagram. Since there are six equations, there are six characteristics. This is illustrated in Figure 2.

The first, third and last characteristics may be related to the waves propagating in the solid matrix. The second, fourth and fifth may be related to the waves propagating in the fluid saturating the void space. The first and second waves are equivalent to rarefaction waves, the third and fourth are equivalent to contact waves and the final two waves, five and six, are equivalent to shocks.

The Roe Riemann solver mentioned in the above section was applied to facilitate the calculation of the flux jumps across the waves. Roe's method relies on the introduction of a parameter vector to convert a non-linear system into a linear system. For the six equation system (A1), this vector takes the form

$$\mathbf{Q} = \begin{bmatrix} q_1 \\ q_2 \\ q_3 \\ q_4 \\ q_5 \\ q_6 \end{bmatrix} = \frac{\mathbf{U}}{\sqrt{r_f}} = \frac{1}{\sqrt{r_f}} \begin{bmatrix} r_f \\ r_s \\ m_f \\ m_s \\ E_f \\ E_s \end{bmatrix} \tag{A11}$$

The arithmetic mean of $\mathbf{Q}$ across the left and right known states ($\mathbf{U}_L$ and $\mathbf{U}_R$) is then introduced into the Jacobian matrix. The resulting matrix is expressed in terms of Roe averaged variables. These are calculated based on the following equation:

$$\tilde{u} = \frac{q_{1L}x_L + q_{1R}x_R}{q_{1L} + q_{1R}} = \frac{\sqrt{r_{fL}}x_L + \sqrt{r_{fR}}x_R}{\sqrt{r_{fL}} + \sqrt{r_{fR}}} \tag{A12}$$

where x_L and x_R are known left- and right-state flow variables. This results in system (A1) being recast in the form

$$\mathbf{U}_t + \tilde{\mathbf{A}}\mathbf{U}_x = \mathbf{Q} \tag{A13}$$

where $\tilde{\mathbf{A}}$ is the Roe averaged Jacobian matrix, which takes the same form as matrix (A3). The Roe averaged eigenvalue, eigenvectors and wave strengths may be written in terms of the Roe averaged quantities, based on Equation (A12).

Levy *et al.* [8] presented the Roe averaged wave strengths, which have been validated using *Mathematica*. The resulting values of $\tilde{\alpha}_j$, for values of j from one to six (one for each wave in the solution), are shown below

$$\tilde{\alpha}_1 = \frac{C_3 - C_4}{2} + \frac{(\rho_s - (\rho_s - \tilde{r}_s)T^*)\tilde{a}_f^2((\tilde{a}_s + \tilde{V}_f - \tilde{V}_s)C_1 + \tilde{a}_f C_2)}{2(\rho_s - \tilde{r}_f)T^*\tilde{a}_s(\tilde{a}_s - \tilde{\zeta}_1)(\tilde{a}_s + \tilde{\zeta}_2)} \tag{A14a}$$

$$\tilde{\alpha}_2 = \frac{(C_1 - C_2)}{2} \tag{A14b}$$

$$\tilde{\alpha}_3 = \Delta r_s - C_3 \tag{A14c}$$

$$\tilde{\alpha}_4 = \Delta r_f - C_1 \tag{A14d}$$

$$\tilde{\alpha}_4 = \frac{(C_1 + C_2)}{2} \tag{A14e}$$

$$\tilde{\alpha}_1 = \frac{C_3 + C_4}{2} + \frac{(\rho_s - (\rho_s - \tilde{r}_s)T^*)\tilde{a}_f^2((\tilde{a}_s - \tilde{V}_f + \tilde{V}_s)C_1 + \tilde{a}_f C_2)}{2(\rho_s - \tilde{r}_f)T^*\tilde{a}_s(\tilde{a}_s + \tilde{\zeta}_1)(\tilde{a}_s - \tilde{\zeta}_2)} \tag{A14f}$$

where the C_n are described by

$$C_1 = \frac{(\gamma - 1)T^*(\Delta E_f + \frac{1}{2}\tilde{V}_f^2 \Delta r_f - \tilde{V}_f \Delta m_f)}{\tilde{a}_f^2} \tag{A15a}$$

$$C_2 = \frac{\Delta m_f - \tilde{V}_f \Delta r_f}{\tilde{a}_f} \tag{A15b}$$

$$C_3 = \frac{E_T(\Delta E_s + (\tilde{V}_s^2 - \tilde{H}_s + \tilde{r}_s\tilde{a}_s^2/E_T)\Delta r_s - \tilde{V}_s \Delta m_s)}{\tilde{r}_s\tilde{a}_s^2} \tag{A15c}$$

$$C_4 = \frac{\Delta m_s - \tilde{V}_s \Delta r_s}{\tilde{a}_s} \tag{A15d}$$

REFERENCES

1. Biot MA. Theory of propagation of elastic waves in a fluid saturated porous solid. *Journal of Acoustical Society of America* 1956; **28**:179–191.
2. Rogg B, Hermann D, Adomeit G. Shock induced flow in a porous medium. *Proceedings of Euromech* 1981; **143**:3–9.
3. Ergun S. Fluid flow through packed columns. *Chemical Engineering Progress* 1952; **48**:89–94.
4. Sorek S, Bear J, Ben-Dor G, Mazor G. Shock waves in saturated thermoelastic porous media. *Transport in Porous Media* 1992; **9**:3–13.
5. Bear J, Bachmat Y. *Introduction to Modelling of Transport Phenomena in Porous Media*. Kluwer: Dordrecht, 1990.
6. Levy A, Sorek S, Ben-Dor G, Bear J. Evolution of the balance equations in saturated thermoelastic porous media following abrupt simultaneous changes in pressure and temperature. *Transport in Porous Media* 1995; **21**:241–268.

7. Bear J, Sorek S, Ben-Dor G, Mazor G. Displacement waves in saturated thermoelastic porous media. I. Basic equations. *Fluid Dynamic Research* 1992; **9**:155–164.
8. Levy A, Ben-Dor G, Sorek S. Numerical investigation of the propagation of shock waves in rigid porous materials: development of the computer code and comparison with experimental results. *Journal of Fluid Mechanics* 1996; **324**:163–179.
9. Ben-Dor G, Levy A, Sorek S. Numerical investigation of the propagation of shock waves in rigid porous materials. Solution of the Riemann problem. *International Journal for Numerical Methods in Heat and Fluid Flow* 1997; **7**:801–813.
10. Levy A, Ben-Dor G, Skews BW, Sorek S. Head-on collision of normal shock waves with rigid porous materials. *Experiments in Fluids* 1993; **15**:183–190.
11. Harten A. High resolution schemes for hyperbolic conservation laws. *Journal of Computational Physics* 1983; **49**:357–393.
12. Toro EF. *Riemann Solvers and Numerical Methods for Fluid Dynamics. A Practical Introduction*. Springer: Berlin, 1999.

